1 **Title**

2 **MerMAIDs: A novel family of metagenomically discovered, marine, anion-conducting and**

3 **intensely desensitizing channelrhodopsins.**

4 **Authors**

5 Johannes Oppermann[1], Paul Fischer[1], Arita Silapetere[1], Bernhard Liepe[1], Silvia Rodriguez-

6 Rozada[2], José Flores-Uribe[3,4], Enrico Peter[1], Anke Keidel[5], Johannes Vierock[1], Joel Kaufmann[6],

7 Matthias Broser[1], Meike Luck[1], Franz Bartl[6], Peter Hildebrandt[5], J. Simon Wiegert[2], Oded Béjà[3],

8 Peter Hegemann[1]*, & Jonas Wietek[1]*

9 [1]Institute for Biology, Experimental Biophysics, Humboldt-Universität zu Berlin, Invalidenstraße

10 42, 10115 Berlin, Germany

11 [2]Research Group Synaptic Wiring and Information Processing, Center for Molecular Neurobiology

12 Hamburg, Falkenried 94, 20251, Hamburg, Germany

13 [3]Faculty of Biology, Technion – Israel Institute of Technology, Haifa 32000, Israel

14 [4]Department of Plant Microbe Interactions, Max Planck Institute for Plant Breeding Research,

15 Cologne 50829, Germany

16 [5]Institute for Chemistry, Physical Chemistry / Biophysical Chemistry, Technische Universität

17 Berlin, Straße des 17. Juni 135, 10623, Berlin Germany

18 [6]Institute for Biology, Biophysical Chemistry, Humboldt-Universität zu Berlin, Invalidenstraße 42,

19 10115 Berlin, Germany

20 *Corresponding authors. Email: hegemann@rz.hu-berlin.de (P.H.); jonaswietek@gmail.com

21 (J.W.)

Abstract

23   Channelrhodopsins (ChRs) are algal light-gated ion channels widely used as optogenetic tools for

24   manipulating neuronal activity. ChRs desensitize under continuous bright-light illumination,

25   resulting in a significant decline of photocurrents. We describe a novel, metagenomically identified

26   family of phylogenetically distinct anion-conducting ChRs (designated MerMAIDs). MerMAIDs

27   almost completely desensitize during continuous illumination due to accumulation of a late non-

28   conducting photointermediate that disrupts the ion permeation pathway. MerMAID desensitization

29   can be fully explained by a single photocycle in which a long-lived desensitized state follows the

30   short-lived conducting state. A conserved cysteine is the critical factor in desensitization, as its

31   mutation results in recovery of large stationary photocurrents. The rapid desensitization of

32   MerMAIDs enables their use as optogenetic silencers for transient suppression of individual action

33   potentials without affecting subsequent spiking during continuous illumination. Our results could

34   facilitate the development of further novel optogenetic tools from metagenomic databases and

35   enhance general understanding of ChR function.

36   Channelrhodopsins (ChRs) are members of the microbial rhodopsin family that directly translate

37   absorbed light into ion fluxes along electrochemical gradients across cellular membranes by

38   opening a conductive pore[1–3]. ChRs are composed of seven transmembrane helices and an

39   embedded retinal cofactor linked to a conserved lysine in helix 7 via a Schiff base (retinal Schiff

40   base, RSB). Upon photon absorption, the RSB isomerizes from all-*trans* to 13-*cis*, which induces

41   structural changes, collectively described as spectroscopically distinguishable intermediates in a

42   photocycle[4].

43   In response to extended light pulses, the photocurrents of most known ChRs decline from an initial

44   peak current to a lower, stationary level, a phenomenon known as desensitization (also termed

45   inactivation)[2,4–6]. The degree and kinetics of desensitization differ among ChRs and depend on

46   pH, membrane voltage as well as light intensity and color, with typically ≤70% amplitude

47   reduction[1,2,7]. Photocurrent decrease via desensitization has been explained by accumulation of

48   late non-conducting photocycle intermediates and by an alternative photocycle exhibiting low

49   cation conductance[7–10].

50   During the past fourteen years, cation-conducting ChRs (CCRs) were widely employed to

51   depolarize genetically targeted neurons or neuronal networks using light to trigger action-potential

52   firing[11–15]. Originally, light-driven microbial ion pumps were utilized to suppress neuronal activity

53   by hyperpolarization[16,17]. Since ion pumps always transport one ion per absorbed photon, efficient

54   neuronal silencing required high ion pump expression levels and continuous, intense illumination.

55   This disadvantage was overcome by converting CCRs into anion-conducting ChRs (ACRs)[18–21].

56   Such engineered ACRs (eACRs)[22] and later-discovered natural ACRs (nACRs)[23–26] silence

57   neuronal activity by light-induced shunting-inhibition, similar to endogenous GABA- or glycine-

58   activated chloride channels[22,27–30].

59   Here, we report a new family of phylogenetically distinct ChRs metagenomically identified from

60   marine microorganisms. These ChRs conduct anions but exhibit unique desensitization in

3

61   continuous light and were therefore designated MerMAIDs (Metagenomically discovered, Marine,

62   Anion-conducting and Intensely Desensitizing ChRs). Seven MerMAIDs were characterized

63   biophysically via electrophysiological recordings, and we elucidated the molecular mechanism of

64   the first accessible MerMAIDs using spectroscopic analyses and molecular dynamic (MD)

65   calculations. We also explore the optogenetic inhibitory potential in neurons.

66   **Results**
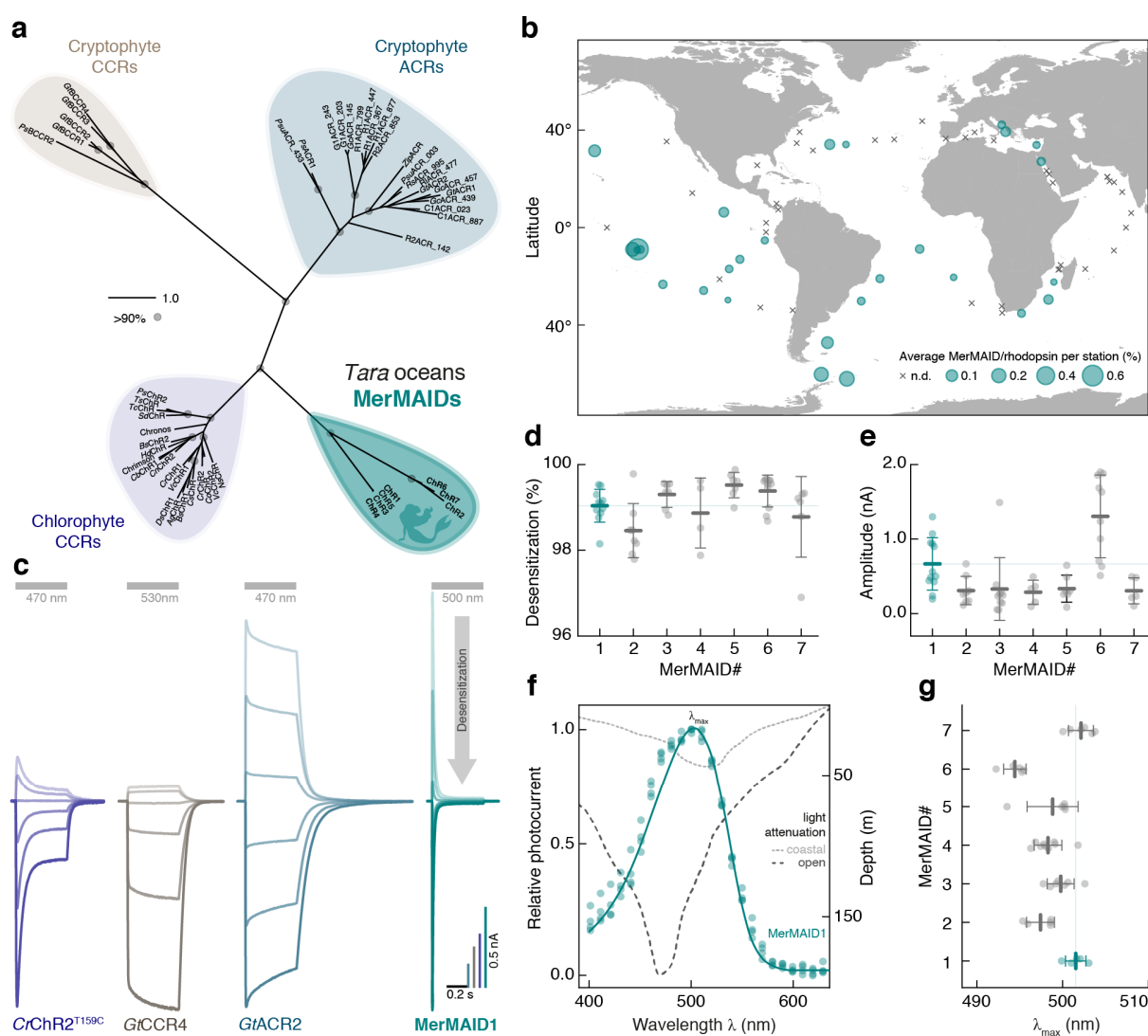
68   **Fig. 1 | Discovery and electrophysiological features of MerMAIDs. a**, Unrooted phylogenetic
69   tree of the channelrhodopsin superfamily, with grey circles representing bootstrap values >90%.
70   Scale bar indicates the average number of amino acid substitutions per site. CCR, cation-

4

71 conducting channelrhodopsin; ACR, anion-conducting channelrhodopsin. **b,** Distribution and
72 relative abundance of MerMAIDs in samples from the *Tara* Oceans project. Area of each circle
73 indicate the estimated average abundance of MerMAID-like rhodopsins at different *Tara* Oceans
74 stations. Stations were MerMAIDs were not detected (n.d.) are indicated by crosses. **c,**
75 Photocurrent traces of representative members of previously identified ChR families and
76 MerMAIDs, recorded from −60 to +40 mV in steps of 20 or 15 mV (*Gt*CCR4). Grey bars indicate
77 light application at denoted wavelengths. **d, e,** Desensitization (**d**) and peak current amplitudes
78 (**e**) of all MerMAIDs at −60 mV during continuous illumination with 500 nm light. **f,** Normalized
79 action spectrum of MerMAID1. Single measurements are shown as dots (n=4), and solid line
80 represents fitted data. Dashed lines indicate light penetration depth in coastal and open seawater
81 (adopted from ref.[86]). λ_{max}, maximum response wavelength; **g,** λ_{max} for all MerMAIDs. Mean values
82 (thick lines) ± standard deviation (whiskers) are shown, and single-measurement data points are
83 represented as dots.

84 Seven putative ChRs constituting a new distinct phylogenetic branch in the ChR superfamily were

85 identified in contigs assembled from the *Tara* Oceans metagenomes (MerMAIDs in Fig. 1a).

86 However, the shortness of the assemblies (<10 kb) precluded taxonomic classification of the

87 contigs. These MerMAIDs appeared to be globally distributed in the oceans, most abundant at

88 stations near the equatorial Pacific and South Atlantic Oceans (Fig. 1b). The MerMAIDs were

89 primarily constrained to the photic zone (depth, 0–200 m), as previously reported for other

90 rhodopsins[31] (Fig. S1).

91 Phylogenetically, the MerMAIDs appear more closely related to chlorophyte CCRs than

92 cryptophyte ACRs (Fig. 1a). However, sequence comparisons indicated that MerMAIDs might be

93 anion-conducting due to the lack of typical glutamate residues found in chlorophyte CCRs, though

94 also missing in chryptophyte CCRs (Fig. S2). To examine their function, we expressed MerMAIDs

95 in human embryonic kidney (HEK) cells and performed whole-cell voltage-clamp experiments at

96 1-day post transfection.

97 When excited with 500-nm light, MerMAID-expressing cells exhibited large photocurrents but in

98 contrast to all previously analyzed ChRs (Fig. 1c), MerMAIDs reveal almost complete

99 desensitization with continuous, bright light exposure (Figs. 1c,d and S3a,b). Maximum peak

100 photocurrent amplitudes reached up to 2 nA (MerMAID-6, Figs. 1e and S3c), but the current did

5

101   not saturate even at 10 mW/mm^2 (Fig. S3d). Transient photocurrent action spectra were recorded

102   to determine the wavelength sensitivity of the MerMAIDs. All variants tested exhibited typical

103   rhodopsin spectra, with maximal sensitivity close to 500 nm (Figs. 1f,g and S3e), as expected for

104   marine organisms, given that blue light penetration is strongest within the photic zone in seawater

105   (Fig. 1f).

106
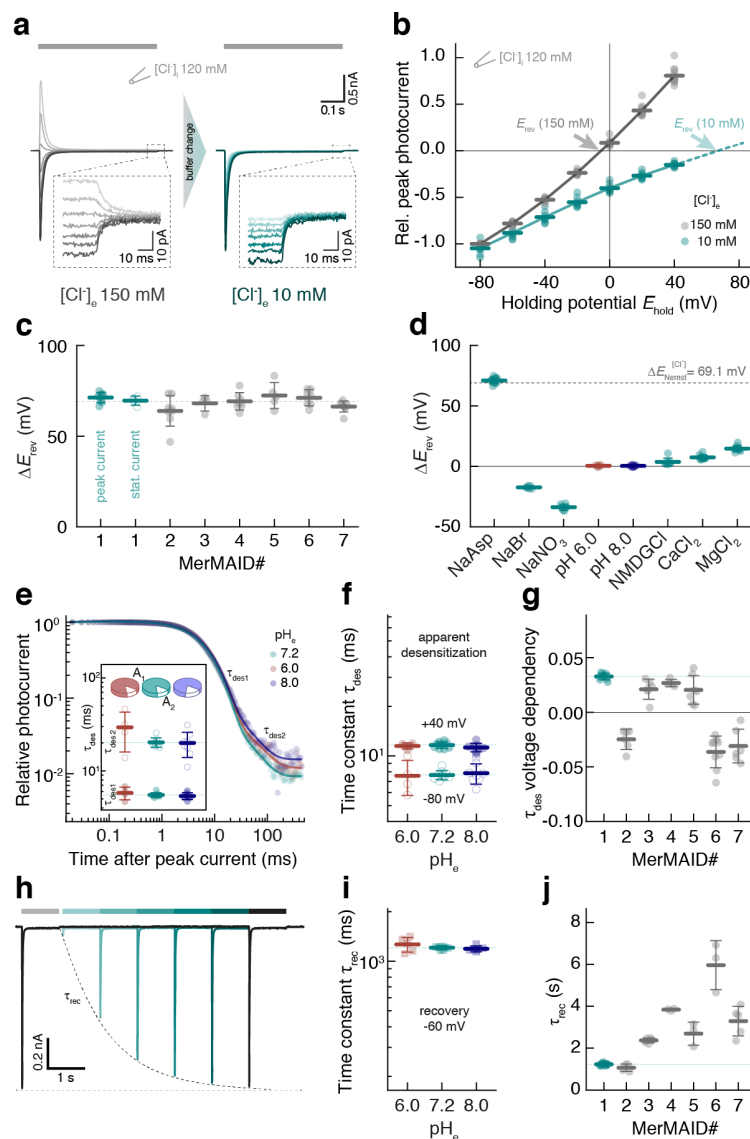
Fig. 2 | Ion selectivity and kinetic properties of MerMAIDs. a, Representative photocurrent
traces of MerMAID1 elicited with 500 nm light (grey bar) at different holding potentials (−80 to
+40 mV, in 20-mV steps, from bottom to top) before (left, grey) and after extracellular chloride
reduction (right, cyan), as indicated. Insets show enlarged views of the remaining stationary

6

111 photocurrent. **b,** Current-voltage relationship of the MerMAID1 peak photocurrent at 150 mM
112 (grey) and 10 mM (cyan) extracellular chloride ($[Cl^-]_e$). Arrows indicate reversal potentials (E_{rev}).
113 **c,** Reversal potential shifts (ΔE_{rev}) upon reduction of $[Cl^-]_e$ for peak currents of all MerMAIDs as
114 well as the stationary current of MerMAID1. **d,** ΔE_{rev} values of MerMAID1 upon exchange of
115 external buffer. ΔE_{rev} of the theoretical Nernst potential for Cl^- is indicated as a dashed line (**c, d**).
116 **e,** Extracellular pH (pH_e) dependence of biphasic MerMAID1 desensitization kinetic. Inset shows
117 the time constants and their relative amplitudes to total decay. **f,** pH_e dependency of the apparent
118 desensitization time constant (τ_{des}) at −80 and +40 mV. **g,** Voltage dependency of τ_{des} for all
119 MerMAIDs in ms/mV. **h,** Double-light pulse experiment at −60 mV and pH_e 7.2 to determine the
120 peak current recovery time constant (τ_{rec}). **i,** pH_e dependency of MerMAID1 at −60 mV. **j,** Recovery
121 time constants of all MerMAID variants. Mean values (thick lines) ± standard deviation (whiskers)
122 are shown, and single-measurement data points are represented as dots.

123 Next, we tested the ion selectivity of the MerMAIDs. Because we suspected anion selectivity, we

124 depleted the extracellular Cl^- from 150 mM to 10 mM while maintaining the intracellular Cl^- at

125 120 mM (Fig. 2a). This increased the inward current and induced an upshift of the reversal

126 potential (Fig. 2a,b), consistent with a Cl^- efflux. A similar shift close to the calculated Cl^--Nernst

127 potential was obtained for all MerMAIDs (Figs. 2c and S4a), as well as for the small stationary

128 photocurrents of MerMAID1 (Figs. 2a,c and S4a). These data justified the classification of

129 MerMAIDs as ACRs.

130 To evaluate the conductance of other anions, we performed ion substitution experiments using

131 MerMAID1 as a model. Replacement of Cl^- with Br^- or NO_3^- resulted in negative reversal potential

132 shifts (Figs. 2d and S4b), thus revealing nonselective anion conductivity, as previously reported

133 for other ACRs[21,23]. In contrast, substitution of Na^+ with $NMDG^+$, Ca^{2+}, or Mg^{2+} had only a slight

134 effect on reversal potentials (Fig. 2d and S4b), thereby excluding a substantial contribution by

135 cations as charge carriers.

136 Rhodopsin function often commonly involves de- and reprotonation of internal amino acids, and

137 pH changes can significantly affect photocurrent amplitude and kinetics[4,9,18,19]. We therefore

138 investigated the effect of extra- and intracellular pH (pH_e and pH_i) changes on MerMAID1.

139 Variation of pH_e between 6.0 and 8.0 slightly altered the photocurrent amplitude (Fig. S4c) but not

140 the reversal potential (Figs. 2d and S4d), thus excluding proton transport. Neither pH_i nor pH_e

7

141   affected the desensitization time constant, τ_{des} (Figs. 2e,f and S4e-g). However, τ_{des} exhibit a

142   moderate voltage dependence (Figs. 2f,g and S4e,f). For MerMAID1,3-5, desensitization slowed

143   down with increasing holding potential whereas τ_{des} was accelerated for MerMAIDs 2, 6, and 7

144   (Fig. 2g). These groups correlated well with the two phylogenetic branches within the MerMAID

145   family (Fig. 1a), although the underlying molecular determinants of this difference remain

146   unknown.

147   To assess the photocycle turnover time (recovery kinetic time constant, τ_{rec}), we performed

148   double-pulse measurements at −60 mV (Fig. 2h) at different pH_e values. The peak current

149   recovered with τ_{rec}=1.21 ± 0.03 s for MerMAID1, and was unaffected by pH_e or pH_i changes

150   (Figs. 2i,j and S4h,i). Between the different MerMAIDs, τ_{rec} varied between 1.1 ± 0.2 s

151   (MerMAID2) and 6 ± 1 s (MerMAID6, Figs. 2j, and S4i).

152   To elucidate the desensitization mechanism, recombinant MerMAID1 was purified from *Pichia*

153   *pastoris* and analyzed by UV/vis and vibrational spectroscopy. Steady-state UV/vis absorption

154   spectra of dark-adapted MerMAID1 exhibited a prominent peak at 502 nm, consistent with the

155   photocurrent action spectra (Fig. 3a). Upon continuous illumination with green light, the 502-nm

156   dark-state absorption peak decreased, while a fine-structured, blue-shifted intermediate with sub-

157   maxima at 346, 364, and 384 nm accumulated in parallel (Fig. 3a,d). Similarly, alkalization

158   converted dark-adapted MerMAID1 into a more red-shifted, fine-structured UV-absorbing species,

159   consistent with a deprotonated 13-*cis* isomer in the M-state and deprotonated all-*trans* RSB dark

160   state[32] that occurs with a pK value of approximately 9.8 (Figs. 3b,d and S5d).

8

161
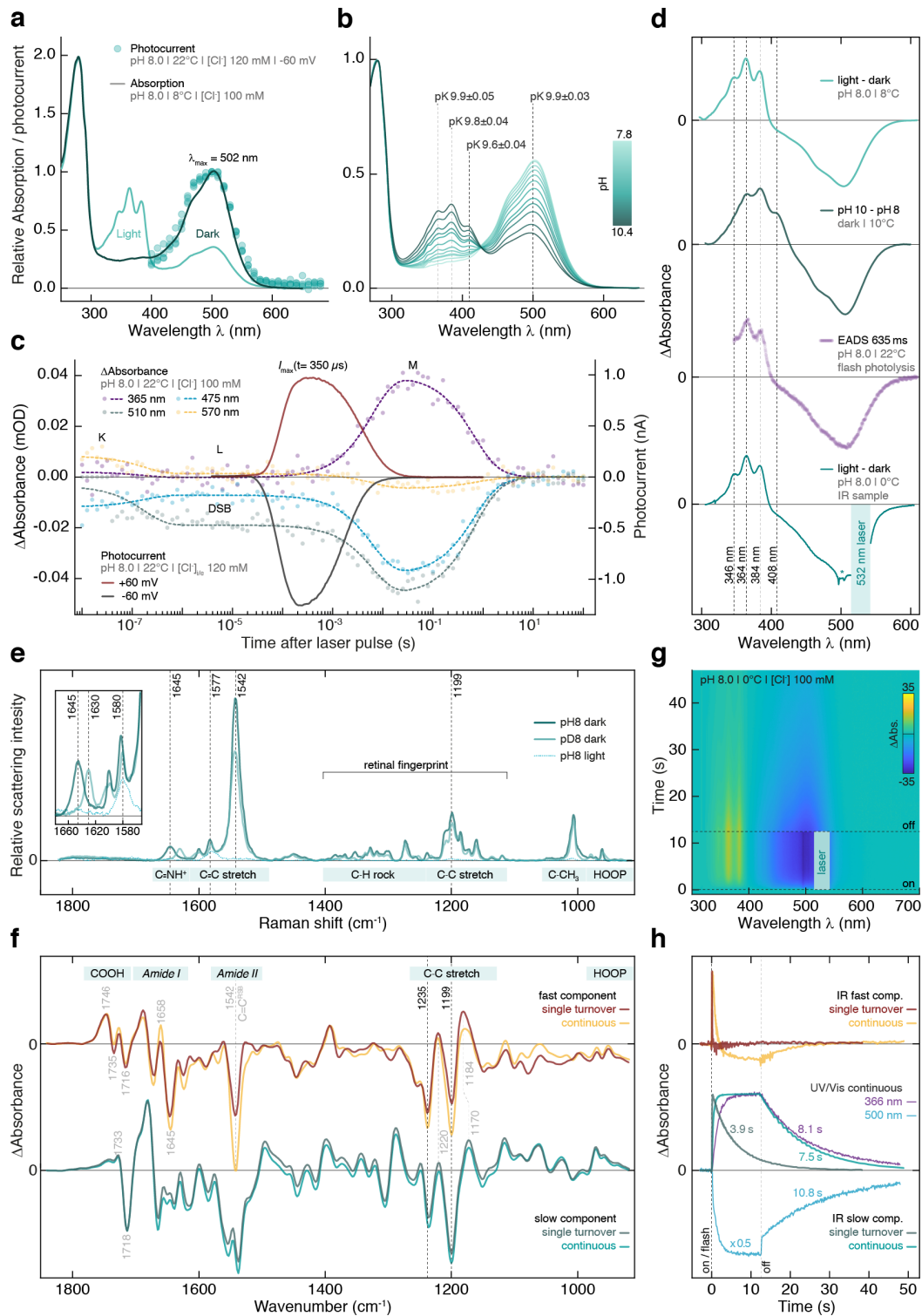
Fig. 3 | Spectroscopic characterization of purified MerMAID1. a, Normalized UV/vis absorption spectra of dark-adapted and illuminated MerMAID1. Filled circles indicate single-measurement action spectra recordings, as shown in Figure 1f. **b,** Normalized UV/vis absorption spectra of

165 MerMAID1 at different pH values, titrated from pH 7.8 to 10.4. The pK values for specific
166 wavelengths are indicated. **c,** Transient absorption changes and electrophysiological recordings
167 obtained with single-turnover laser pulse excitation. **d,** Fine-structured difference absorption
168 spectra obtained from different experiments. (From top to bottom) light minus dark difference
169 spectra obtained from data shown in panel a, pH-difference spectra calculated from panel b data,
170 evolution-associated difference spectra (EADS) resulting from a global fit of the transient
171 absorption spectra and (bottom) light-minus-dark difference spectrum measured using the FTIR
172 sample shown in (**g**). Due to strong laser scattering, a portion of the spectral data is excluded for
173 the FTIR sample, and residual scattering is marked with an asterisk. **e,** Resonance Raman spectra
174 of dark-adapted MerMAID1 at pH/D 8 (recorded at 488 nm) as well as cryo-trapped and
175 illuminated protein sample at pH 8 (recorded at 413 nm). Inset: zoomed $C=NH^+$ stretching region.
176 **f,** Kinetically decomposed FTIR light-minus-dark absorption of MerMAID1, recorded with single
177 turnover and continuous illumination at 0°C. Bands marked in grey are discussed in the
178 Supplementary Material **g,** Contour plot of transient absorption changes of the sample used in (**f**)
179 illuminated with a 532 nm continuous laser. **h,** Decay kinetics of the fast and slow FTIR
180 components obtained under single-turnover and continuous illumination conditions, respectively.
181 Kinetics at 366 and 500 nm obtained from the UV/vis spectroscopic measurements shown in (**g**)
182 are shown for comparison.

183 Single-turnover voltage-clamp experiments showed a maximum channel conductance 350 μs

184 after ns-pulse laser excitation. Channel closing was biphasic, with a dominant fast component and

185 an apparent closing time constant (τ_{off}) of 2.7 ± 0.1 ms (Figs. 3c and S5a). Transient UV/vis

186 absorption spectra (Figs. 3c and S5b,c) revealed an early decaying (173 ns) K-like photoproduct

187 observed only briefly on our time scale. The evolution-associated difference spectrum (EADS) of

188 the subsequent L-intermediate is slightly blue shifted and to some extent broadened compared to

189 the dark-state spectrum (Fig. S5c), indicating closer proximity of the primary counterion to the

190 RSBH⁺ immediately prior to RSB deprotonation[33]. Within 6 ms, the L-state converted to the M-

191 state, with concomitant deprotonation of the RSB, as indicated by the large blue shift coinciding

192 with channel closure (Figs. 3c and S5a,b). The transient M-state EADS was similarly fine-

193 structured as observed for continuous photo activation (Fig. 3d), indicating accumulation of the M-

194 state during sustained light exposure.

195 To assess potential retinal chromophore isoforms of MerMAID1, we performed resonance Raman

196 (RR) spectroscopy at 80 K. Excitation of dark-adapted MerMAID1 at 488 or 514 nm produced

197 identical RR spectra (Fig. S5e), indicating structural homogeneity of the chromophore. The

10

198   vibrational band pattern in the retinal fingerprint region (1100–1400 cm^{-1}) was characteristic of an

199   all-*trans* RSB[34,35] (Fig. 3e). Upon proton/deuterium exchange, the C=N stretching mode

200   downshifted from 1645 to 1630 cm^{-1} (inset Fig. 3e), indicative of a weakly hydrogen-bonded[36]

201   protonated RSB[34,35]. RR spectra of photoactivated MerMAID1 cryo-trapped in the M-state and

202   excited at 413 nm exhibited a prominent band at 1577 cm^{-1} attributable to a 13-*cis* configuration

203   of the chromophore with deprotonated RSB[37]. RR spectra of dark-adapted MerMAID1 probed with

204   488 or 413 nm at pH 10 were similar to spectra of dark- and light-adapted MerMAID1 at pH 8 (Fig.

205   S5e). Notably, strong bands in the C=C stretching region at ca. 1540 and 1577 cm^{-1} indicated a

206   mixture of two chromophore isomers, corresponding to the protonated and deprotonated all-*trans*

207   RSB of the dark state at high pH. Thus, RR spectra confirmed that MerMAID1 undergoes all-*trans*

208   to 13-*cis* retinal isomerization and deprotonation of the RSB during illumination and may

209   deprotonate at high pH in the dark.

210   Time-resolved Fourier-transform infrared (FTIR) spectra were collected at pH 8.0 and 0 °C to

211   examine the light-driven molecular processes of MerMAID1 under single-turnover conditions and

212   continuous illumination (Fig. 3f,h), with parallel UV/vis observation of M-state formation (Fig. 3g,

213   h). Kinetic decomposition of light-dark FTIR difference spectra revealed highly similar fast and

214   slow spectral components for both single-turnover and continuous illumination, respectively

215   (Fig. 3f). At both conditions, the slow FTIR component relaxed to the dark state mono-

216   exponentially, within seconds (Fig. 3h) and was assigned to the late M-state that accumulated with

217   continuous illumination (Fig. 3g,h) without formation of other photoproducts. This assignment was

218   supported by data for the retinal fingerprint region that—similar to the RR data—indicated all-*trans*

219   to 13-*cis* retinal isomerization as the only photoreaction based on the negative bands at 1235(−)

220   and 1199(−) cm^{-1}. The fast FTIR spectral components resembled the short-lived conducting L-

221   state preceding the late M-intermediate, as inferred from the comparable decay kinetics (see

222   Supplemental Discussion).

11
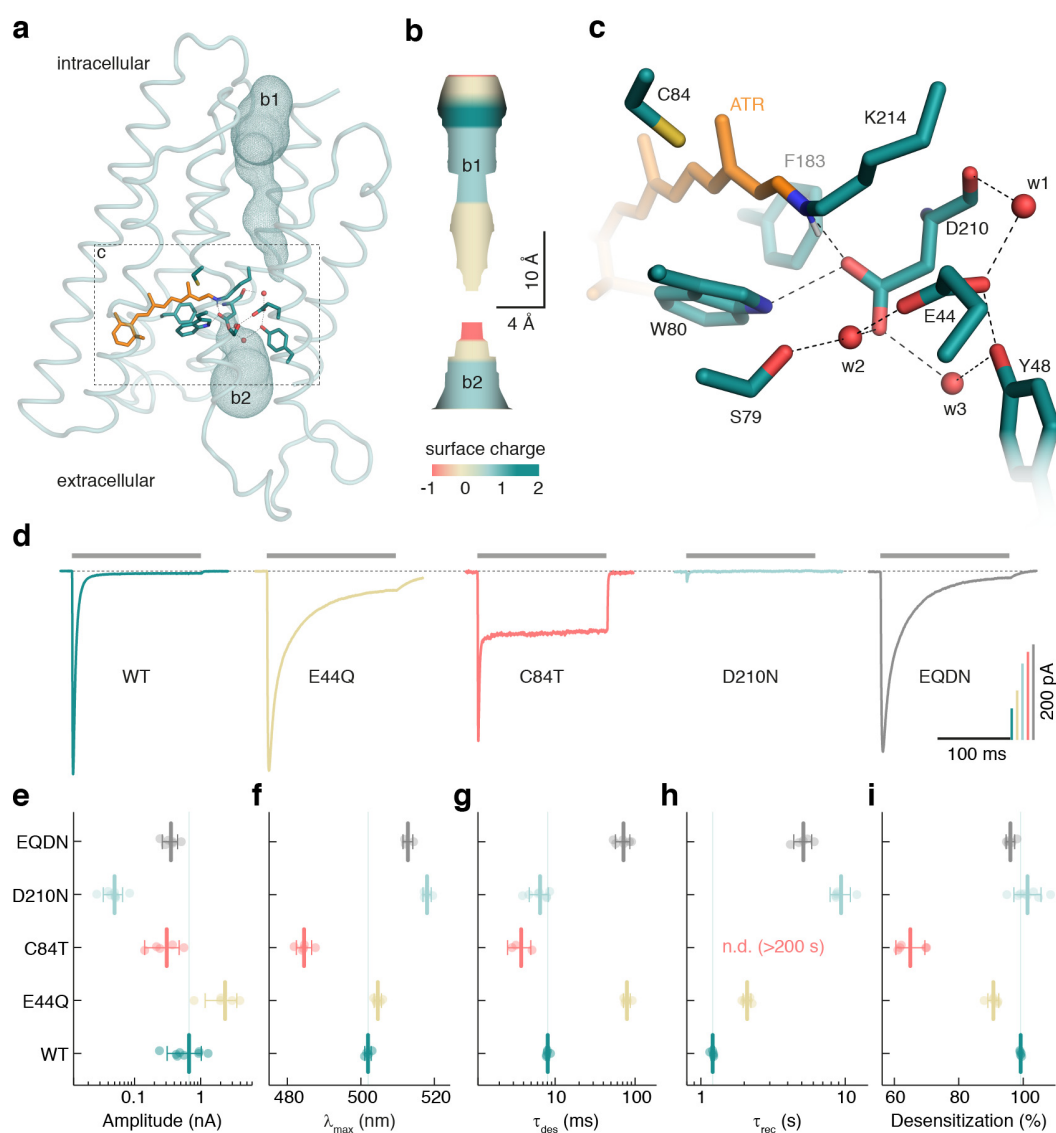
Fig. 4 | MD simulations and mutational analysis of MerMAID1. a, Overview of the MD simulation homology model of MerMAID1 in the dark. The predicted ion permeation pathway is shown as mesh (b1, b2), and ribbons represent the protein backbone. **b,** Electrostatic surface potential of the predicted chloride permeation pathway. **c,** Detailed view of the active-site residues, with amino acids shown as cyan sticks and the all-*trans* retinal (ATR) in orange. Red spheres denote water molecules that remained stable during MD simulation. **d,** Representative photocurrent traces of wild-type (WT) MerMAID1 and selected MerMAID1 mutants recorded at −60 mV. Photocurrent amplitudes (**e**), λ_{max} (**f**), apparent τ_{des} of the peak current (**g**), recovery time constant, τ_{rec} (**h**), and extent of desensitization (**i**) of WT MerMAID1 and indicated mutants. Mean values (thick lines) ± standard deviation (whiskers) are shown, and single-measurement data points are represented as dots.

12

235   Site-directed mutagenesis guided by MD simulations and probed by electrophysiological

236   recordings were conducted to further examine the molecular mechanism for the intense

237   desensitization of the MerMAIDs. For MD simulations, a MerMAID1 homology model was

238   constructed based on the iC++ crystal structure[38] and embedded in a phospholipid bilayer (Figs.

239   4a and S6a). The D210, E44, W80, and Y48 side chains located near the protonated Schiff base

240   (Fig. 4a,c) maintained their relative positions during a 100-ns MD simulation. The orientation and

241   distances of these residues changed only slightly with inflowing water (Fig. S6d-f). Possible ion

242   translocation pathways were calculated using MOLEonline[39]. Figure 4a,b shows the most likely

243   ion pathway based on surface charge considerations (Fig. S6b,c). Extracellularly, MerMAID1 is

244   accessible via a narrowing tunnel that is disrupted by W80, D210, and the RSB (Fig. 4a,b).

245   Intracellularly, another ion pathway is formed leading from the protein surface almost to the Schiff

246   base, disconnected only by a short hydrophobic barrier. In our model, the carboxylic residues of

247   the active site complex (E44 and D210) were deprotonated based on pK_a calculations (Fig. 4c,

248   pK_a <5.5). D210, which acts as closest counterion (2.6 Å) to the Schiff base nitrogen, primarily

249   stabilizes the RSB proton (Fig. 4c). The carboxyl group of D210 also interacts with S79, Y48, and

250   E44 via two water molecules, whereas E44 hydrogen bonds directly to Y48 and is linked to the

251   backbone oxygen of D210 via another water molecule (Fig. 4c). When the counterion D210 is

252   neutralized (D210N), photocurrents are drastically reduced (Fig. 4d,e), λ_{max} was 16 nm red-shifted

253   (Fig. 4f), and the recovery kinetics decelerated markedly (Fig. 4h). Elimination of the more distant

254   E44 via an E44Q mutation caused only a 3 nm bathochromic action-spectrum shift (Fig. 4f),

255   increased the photocurrent amplitudes (Fig. 4f), decelerated desensitization by a factor of 10

256   (Fig. 4d,g) and slightly reduced the extent of desensitization (Fig. 4i). Replacement of both acidic

257   residues (E44Q-D210N) only halved photocurrent amplitudes (Fig. 4e) and shifted λ_{max} to

258   513 ± 1 nm (Fig. 4f), suggesting rearrangement of the hydrogen bond network around the RSB.

259   Desensitization remained strong (Fig. 4i), but the kinetics slowed, similar to the E44Q mutation

260   alone (Fig. 4g).

261 Neutralization of E44 increased the stationary current only slightly (Fig. 4i), whereas we identified

262 C84 (the *Cr*ChR2 C128 homolog) as a crucial determinant of the inactivation process. The C84T

263 mutant exhibited a decreased peak current amplitude but markedly increased stationary

264 photocurrent (Fig. 4d,e), resulting in only 65 ± 5 % desensitization (Fig. 4d,i) and minimally altered

265 desensitization kinetics (Fig. 4d,g). In contrast, we observed no peak current recovery within a

266 time period of 200 s. As suggested by our model structure and the pronounced 17 nm blue-shifted

267 λ_{max} (Fig. 4f), C84 is located near the retinal polyene chain and the C13 methyl group (Fig. 4a,c).

268 In MerMAIDs, this cysteine cannot serve as a link between helices 3 and 4 as discussed for

269 bacteriorhodopsin[40,41] and CCRs[42,43] due to the absence of a hydrogen-bonding partner in helix 4

270 (Fig. S2). C84 might stabilize the deprotonated RSB within the anion permeation pathway instead,

271 thereby disrupting further ion conduction via charge repulsion of the deprotonated RSB during the

272 photocycle.
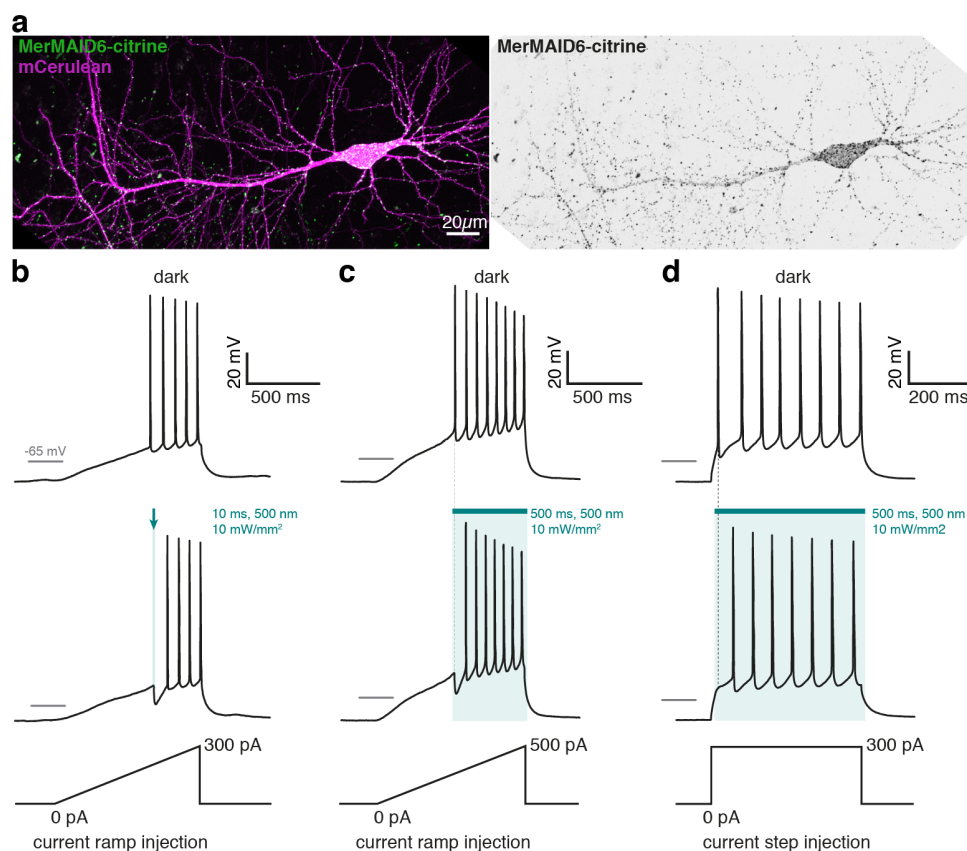
273

274　**Fig. 5 | Neuronal application of MerMAID6 as optogenetic silencer. a,** CA1 pyramidal neuron
275　expressing MerMAID6-Citrine (green) 5 days after electroporation (stitched maximum intensity
276　projections of two-photon images). mCerulean (magenta) was co-electroporated to visualize
277　neuronal morphology (left). Fluorescence intensity shown as inverted gray values (right). **b** and **c**,
278　Voltage traces in response to depolarizing current ramps injected into MerMAID6-expressing CA1
279　pyramidal cells. Illumination with green light (500 nm, 10mW/mm^2) for a brief (10 ms, **b**) or longer
280　(500 ms, **c**) time period blocked single spikes. Light onset preceded action potential onset
281　(measured in the dark condition) by 5 ms. **d,** Same as (**c**) but a depolarizing current step of 300
282　pA was injected into the neuron instead of a current ramp.

283　Finally, we evaluated the utility of MerMAIDs as optogenetic tools for inhibiting neuronal activity.

284　As MerMAID6 exhibited the highest photocurrent in HEK cells (Fig. 1e), we generated a Citrine-

285　labeled MerMAID6 variant and co-expressed it with mCerulean as a volume marker. MerMAID6-

286　Citrine expression was readily detected in CA1 pyramidal neurons of hippocampal slice cultures

287　4 to 5 days after single-cell electroporation. We observed membrane-localized MerMAID6

288　expression, with some fraction of the protein displaying a speckled cellular distribution (Fig. 5a).

289　However, illumination triggered high transmembrane photocurrents with biophysical properties

290　similar to those observed in HEK cells (Fig. S8). The large, transient photocurrents observed in

291　neurons led us to hypothesize that MerMAID6 could be used to block single action potentials (APs)

292　with high temporal precision and without affecting subsequent APs in the presence of light. We

293　first injected a depolarizing current ramp into the soma to precisely determine the rheobase for AP

294　firing in the dark. A 10 ms light pulse synchronized with the first AP that occurred during darkness

295　eliminated generation of this AP (Fig. 5b). We then applied a 500 ms light pulse synchronized to

296　the time of onset of the first AP lasting throughout the remainder of the current ramp (Fig. 5c) or a

297　depolarizing current step (Fig. 5d), MerMAID6 suppressed generation of the first AP, without

298　affecting the following ones due to rapid accumulation of the desensitized and non-conducting

299　state during extended illumination. Similarly, selective inhibition of a single AP was achieved with

300　MerMAID1 (Fig. S7), demonstrating that photoactivated MerMAID1 and 6 provide efficient and

301　temporally precise inhibition of neuronal activity.

302

Discussion

304 We extensively characterized the biophysical properties of the MerMAIDs, a new family of ChRs

305 identified from metagenomic data. All MerMAIDs share similar activity maxima optimal for sensing

306 light in moderate-depth seawater. Similar to other recently discovered natural ACRs[23], MerMAIDs

307 selectively conduct anions. Distinct from all other ChRs, MerMAIDs exhibit almost complete

308 desensitization during exposure to continuous bright light. However, the environmental advantage

309 of near-complete desensitization compared with non-inactivating ACRs is unclear.

310 After photon absorption, the MerMAID1 chromophore isomerizes from all-*trans* to 13-*cis*, as

311 demonstrated by RR and FTIR spectroscopy. We hypothesize that the RSBH$^+$ dipole changes

312 orientation and distance with respect to the nearby D210, as evidenced by formation of the L-

313 intermediate, analogous to bacteriorhodopsin[33]. The K→L transition and formation of the open

314 state is accompanied by minimal protein backbone changes that induce changes in hydrogen

315 bonding and side-chain pK values, presumably involving the active-site residues D210 and E44.

316 Maximum channel conductivity, reached within 350 µs, is UV/vis spectroscopically almost silent.

317 Channel closing proceeds concurrently with RSB deprotonation, leading to M-intermediate

318 formation, similar to cryptophyte ACRs[24,44] but in contrast to chlorophyte CCRs, in which M-state

319 formation precedes channel opening[45,46]. These observations suggest that the positively charged

320 protonated RSB is part of the chloride conducting pathway, consistent with the calculated ion

321 permeation pathway along the counter-ion complex, similar to crystal structures of *Guillardia theta*

322 ACR1 (*Gt*ACR1)[38,47]. Chloride flux in MerMAID1 is interrupted by charge repulsion following

323 deprotonation of the Schiff base. In the final photocycle step, MerMAID1 structurally rearranges,

324 the RSB reprotonates, and the initial dark state is fully repopulated within seconds.

325 The observation that photocurrent kinetics were not affected by intra- or extracellular pH changes

326 suggests that the RSB proton remains within the central active-site complex during the photocycle,

327 as recently reported for heliorhodopsins[31]. D210 is the primary counterion of the RSB in

16

328   MerMAID1, but both carboxylic residues (E44 and D210) participate in de- and reprotonation of

329   the MerMAID1 chromophore, as neutralization of either one or both residues affects formation of

330   the conductive or desensitized state. However, retention of function of the E44Q-D210N double

331   mutant suggests the possibility of alternative proton acceptor and donor sites.

332   The unique desensitization of the MerMAIDs can be explained by the accumulation of the blue-

333   shifted M-intermediate during constant photoactivation. Because the non-conducting M-

334   intermediate is formed within milliseconds and decays only within hundreds of milliseconds, the

335   current declines to 1 % in continuous light. This mechanism is consistent with an M-state that

336   cannot be photochemically converted back to the dark state (Fig. S5g,h). As discussed in previous

337   reports, decline of *Cr*ChR2 photocurrents upon continuous illumination is due to both, the

338   accumulation of late non-conducting photocycle intermediates and population of a parallel (*syn*-)

339   photocycle with an only weakly conducting open state[7–9]. The accumulation of a late photocycle

340   intermediate is the dominant mechanism in MerMAID1, as demonstrated by FTIR spectroscopy;

341   no parallel photocycle is needed to explain the strong inactivation.

342   We found that replacing C84 in MerMAID1 decreases the peak photocurrent but increases

343   stationary photocurrents, thus reducing the extent of desensitization, possibly due to either a

344   prolonged L-state or a shortened recovery from the M- to the initial dark state. C84 could have

345   dual functions in wild-type MerMAID1: i) stabilizing the deprotonated RSB to retain the repulsing

346   charge in the ion pathway and block the channel; ii) suppression of C=N *anti* to *syn* isomerization

347   and population of parallel *syn*-photocycles as discussed for *Cr*ChR2[10].

348   Another unusual feature of MerMAID1 are the fine-structured absorption spectra of both the

349   deprotonated all-*trans* RSB in the dark at alkaline pH and the 13-*cis* retinal of the M-state. Such

350   unusual spectra have been reported for other microbial rhodopsins after retro-retinal formation

351   upon reduction with borohydride[48] or hydrolysis of the RSB[49]. In both cases, the UV fine structure

352   results from immobility of the deprotonated chromophore, which is typically more pronounced at

17

353   deep temperatures[50,51]. Alkalization-induced fine-structured spectra were reported for eACRs[38]

354   and wild-type and mutant nACRs[44] and suggested to result from RSB hydrolysis[38] or protein

355   denaturation[52]. However, in *Gt*ACR1, the covalent bond between the retinal and the Schiff base–

356   forming lysine is not broken at high pH. Instead, the RSB deprotonates and adopts an M-like

357   configuration[53]. RR spectra of MerMAID1 at pH 10 (Fig. S5e) suggested that the retinal is similarly

358   deprotonated and adopts a rigid configuration in all-*trans* instead of 13-*cis*, as in the M-state.

359   MerMAID1 and 6 effectively inhibited neuronal activity with high temporal precision. Due to the

360   unique desensitization of the MerMAIDs under continuous illumination, single APs can be blocked

361   at the onset of illumination without affecting subsequent neuronal spiking. Hence, MerMAIDs could

362   serve as transient optogenetic silencers to inhibit individual APs with high precision in combination

363   with subsequent imaging of spectrally overlapping reporters of neuronal activity. MerMAIDs would

364   thus facilitate continuous monitoring of neuronal activity subsequent to short-duration inhibition at

365   the same wavelength.

366   The identification of the entirely new ChR family fortifies the value of metagenomic data for the

367   discovery of novel photoreceptor proteins potentially applicable as optogenetic tools. The initial

368   in-depth characterization of MerMAIDs will foster the generation of ChRs with novel biophysical

369   properties and lead to deeper understanding of the working principles of rhodopsins.

370   **Methods**

371   *Identification of novel channelrhodopsins and metagenomics data analysis*

372   Novel channelrhodopsin variants were identified using full-length *Cr*ChR1 and *Cr*ChR2 amino acid

373   sequences (GenBank: AAL08946.1, and NCBI reference sequence: XP_001701725.1,

374   respectively) as queries for tblastn 2.6.0 analysis[54] against a database of contigs assembled from

375   the *Tara* Oceans metagenomic datasets of bacterial[55], viral[56], and girus[57] samples. The

376   assemblies were generated as described elsewhere[58].

18

377   MerMAID abundance in the marine environment was estimated using the Ocean Gene Atlas[59]

378   after mining the Ocean Microbial Reference Gene Catalog[55]. A collection of representative

379   microbial rhodopsin protein sequences from distinct subfamilies containing the MerMAIDs was

380   aligned using the MAFFT online server (ver. 7)[60]. The alignment was used to generate a Hidden

381   Markov Model (HMM) using hmmbuild from the HMMER 3.1b2 suite[61]. The HMM served as the

382   query in the Ocean Gene Atlas[59] or an HMMER-based search with default parameters against the

383   Ocean Microbial Reference Gene Catalog. The Ocean Gene Atlas results for abundances and

384   homologs were stored locally for further analysis.

385   Protein homologs from the Ocean Gene Atlas and MerMAIDs were pooled and aligned using the

386   MAFFT web server. MAFFT multiple sequence alignment was used to identify those homologs

387   phylogenetically closer to the MerMAIDs and were tagged as MerMAID-like. Ocean Gene Atlas

388   abundance data were parsed using a custom R script to calculate the ratio of ACR-like proteins

389   to total rhodopsins in each *Tara* Oceans sample. The MerMAID-like/total rhodopsin ratio was

390   coupled with environmental metadata from the *Tara* Oceans samples to generate depth profiles

391   and distribution maps using the R packages maps[62], ggplot2[63], and ggalt[64].

392   The phylogenetic tree was generated using phylogeny.fr[65] and the sequence alignment using

393   Clustal X[66]. The sequence alignment was visualized using the ENDscript 2 web server[67], and the

394   alignment was cropped to include the transmembrane regions of selected ChRs.

395   *Molecular biology and protein purification*

396   Human/mouse codon-optimized sequences encoding MerMAIDs were synthesized (GenScript,

397   Piscataway, NJ) and cloned into the p-mCherry-C1 vector using *Nhe*I and *Age*I restriction sites

398   (FastDigest, Thermo Fisher Scientific, Waltham, MA) for electrophysiologic recordings in HEK293

399   cells. Due to incomplete metagenomic data, a methionine was added as start codon for MerMAID1

400   and MerMAID4. Site-directed mutagenesis was performed using *Pfu* polymerase (Agilent

19

401   Technologies, Santa Clara, CA). MerMAID1 and MerMAID6 cDNAs were subcloned into neuron-

402   specific expression vectors (pAAV backbone, human synapsin promoter) in frame with Citrine

403   cDNA using Gibson assembly[68]. For expression in *Pichia pastoris*, the MerMAID1 gene was

404   subcloned with a C-terminal TEV protease restriction site and a 6× His-Tag into the pPiCZ vector

405   (Invitrogen, Carlsbad, CA). Zeocin™-resistant positive clones were selected from electroporation-

406   transformed yeast cells. Expression of MerMAID1 in precultured cells was induced with

407   2.5% methanol in presence of 5 µM all-*trans* retinal for 24 h. Cells were harvested by

408   centrifugation and resuspended in breaking buffer (50 mM NaPO$_4$, 1 mM EDTA, 1 mM PMSF,

409   5% glycerol [pH 7.4]) and disrupted by high pressure using a French press (G. Heinemann

410   Ultraschall und Labortechnik, Schwäbisch Gmünd, Germany). The membrane fraction was

411   collected, homogenized, and solubilized overnight at 4°C in 100 mM NaCl, 20 mM Tris-HCl,

412   20 mM imidazole, 1 mM PMSF, 5 µM all-*trans* retinal, and 1% (*w/v*) dodecyl maltoside (DDM).

413   Recombinant rhodopsin was purified by affinity chromatography (HisTrap™ FF Crude column, GE

414   Healthcare Life Science, Chicago, IL) and gel filtration (HiPrep™ 26/10 desalting, GE Healthcare

415   Life Science). Before elution, an additional washing step with buffer containing 50 mM imidazole

416   was performed. Purified protein was concentrated and stored in 100 mM NaCl, 20 mM Tris-HCl

417   (pH 8), and 0.05% DDM.

418   *Electrophysiology in HEK293 cells*

419   HEK293 cell culture and electrophysiologic experiments were performed as described

420   previously[22,69]. Cells were supplemented with 1 µM all-*trans* retinal, seeded at a density of

421   1 × 10^5/ml on poly-D-lysine–coated coverslips, and transiently transfected using Fugene HD

422   (Promega, Madison, WI). At 1 to 2 days post-transfection, whole-cell patch-clamp recordings were

423   performed at 24 °C. The resistance of fire-polished patch pipettes was 1.5–2.5 MΩ, and a

424   140 mM NaCl agar bridge served as the reference electrode. Membrane resistance was generally

425   ≥1 GΩ, and the access resistance was <10 MΩ. Signals were amplified (AxoPatch200B), digitized

426   (DigiData400), and acquired using Clampex 10.4 (all from Molecular Devices, Sunnyvale, CA).

427   Light from a Polychrome V (TILL Photonics, Planegg, Germany) with 7 nm bandwidth was

428   channeled into an Axiovert 100 microscope (Carl Zeiss, Jena, Germany) controlled via a

429   programmable shutter system (VS25 and VCM-D1; Vincent Associates, Rochester, NY). Light

430   intensity was measured in the sample plane using a calibrated optometer (P9710; Gigahertz Optik,

431   Türkenfeld, Germany) and calculated for the illuminated field of the W Plan-Apochromat 40×/1.0

432   DIC objective (0.066 mm^2, Carl Zeiss). Final buffer osmolarity was set with glucose to 320 mOsm

433   (extracellular) or 290 mOsm (intracellular), and the pH was adjusted using N-methyl-D-glucamine

434   or citric acid. Liquid junction potentials were calculated (Clampex 10.4) and corrected. For ion

435   selectivity measurements, extracellular buffers (supplementary table S1) were exchanged in

436   random order by adding at least 3 ml to the measuring chamber (volume ~0.5 ml). Fluid level was

437   kept constant using an MPCU bath handler (Lorentz Messgerätebau, Katlenburg-Lindau,

438   Germany). MerMAID photocurrents were induced for 500 ms and recorded between −80 and

439   +40 mV in 20-mV steps. Low-intensity light between 390 and 680 nm was applied in 10-nm steps

440   for 10 ms at −60 mV to generate action spectra. Equal photon irradiance at all wavelengths was

441   achieved using a motorized neutral-density filter wheel (Newport, Irvine, CA) in the light path,

442   controlled by custom software written in LabVIEW (National Instruments, Austin, TX). For light

443   titration experiments, photocurrents were induced for 2 s at −60 mV, and light was attenuated

444   using ND filters (SCHOTT, Mainz, Germany) inserted into the light path using a motorized,

445   software-controlled filter wheel (FW212C, Thorlabs, Newton, NJ). Single-turnover experiments

446   were performed with the above mentioned setup described elsewhere[10,70]. An Opolette HE 355

447   LD Nd:YAG laser/OPO system (OPOTEK, Carlsbad,CA) served as pulsed laser light source.

448   *UV-Vis Spectroscopy*

449   Steady-state absorption spectra were recorded using a Cary 300 UV/vis spectrophotometer

450   (Varian Inc., Palo Alto, USA) or UV-2600 UV/vis spectrophotometer (Shimadzu, Kyōto, Japan) at

451   a spectral resolution of 1 nm in buffer containing 100 mM NaCl, 20 mM Tris, and 0.05% DDM

452   (pH 8). Light-adapted absorption spectra were acquired by illuminating the sample with a 530 nm

453   LED with a 520 ± 15 nm filter. For pH titration experiments, small volumes of 1 M NaOH were

454   added to samples in titration buffer (100 mM NaCl, 10 mM BTP, 10 mM CAPS, 0.05% DDM

455   [pH 7.5]). The pH was measured using pH microelectrodes (SI Analytics, Mainz, Germany). The

456   transient absorption spectroscopic measurements shown in Figure S5b,c were performed as

457   previously reported[24] at 22°C using a modified LKS.60 flash-photolysis system (Applied

458   Photophysics Ltd., Leatherhead, UK). For sample excitation, the laser pulse was tuned to 500 nm

459   using a tunable optical parametric oscillator (MagicPrism, OPOTEK), which was pumped with the

460   third harmonic of a Nd:YAG laser (BrilliantB, Quantel, Les Ulis, France). The laser energy was

461   adjusted to 5 mJ/shot and pulse duration of 10 ns. A 150-W xenon lamp (Osram, München,

462   Germany) was used to monitor changes in absorption. Transient spectra were recorded in multi-

463   wavelength data sets at a resolution of 0.4 nm using an Andor iStar ICCD camera (DH734; Andor

464   Technology Ltd, Belfast, Ireland). Spectra were recorded at 101 different time points between

465   10 ns and 100 s (10 points per decade, isologarithmically). To ensure complete recovery of the

466   dark state, samples were kept in the dark for 120 s before the subsequent recording. For the

467   transient absorption spectra shown in Figure 3h, FTIR samples were used. Spectra were recorded

468   using an Ocean FX array detector (Ocean Optics, Largo, FL) with a spectral resolution of 2.4 nm

469   and integration time of 50 ms. Samples were illuminated using a 50 mW continuous-wave LASER

470   emitting 532-nm light (no. 37028, Edmund Optics, York, UK).

471   *FTIR spectroscopy*

472   To prepare samples for FTIR, 10 µl of initial protein solution (>20 mg/ml, 100 mM NaCl, 20 mM

473   Tris, 0.05% DDM [pH 8]) was dried stepwise on a BaF_2 window under a stream of dry air and

474   subsequently rehydrated. Samples were then sealed with a second BaF_2 window. To ensure

475   constant sample thickness, a 3-µm PTFE spacer was placed between the windows. For

476   deuteration, the protein solution was washed at least five times with deuterium buffer (100 mM

477   NaCl, 20 mM Tris, 0.05% DDM [pD 8]) using Centricon filters and subsequently illuminated using

478   white light to improve deuteration inside the opened channel. FTIR spectra were acquired at 0°C

479   using a Vertex 80v FTIR spectrometer (Bruker Optics, Karlsruhe, Germany) equipped with a liquid

480   nitrogen–cooled MCT detector (Kolmar Technologies, Newburyport, MA). The spectrometer was

481   operated in rapid scan mode with a data acquisition rate of 300 kHz and spectral resolution of

482   8 cm^{-1}. An optical cutoff filter at 1850 cm^{-1} was used in the beamline. After at least 60 min for

483   equilibration, samples were continuously illuminated using a set of green-light LEDs with an

484   emission maximum of 520 nm. Single-turnover illumination was performed using a 10-Hz pulsed

485   Nd:YAG Powerlite 9010 LASER as the pump source for a Horizon II optical parametric oscillator

486   (Continuum, San Jose, CA) set to 530 nm. The pulse width of the setup was approximately

487   5 ± 2 ns, with an energy output of approximately 60 mJ. The time resolution was 6 ms (achieved

488   by operation in forward-backward mode and splitting of the interferogram).

489   *RR spectroscopy*

490   RR spectra were acquired with excitation lines of an Ar$^+$ (514 nm, 488 nm) and Kr$^+$ laser (413 nm)

491   (Coherent, Santa Clara CA). Raman signals were detected in a backscattering configuration

492   (180°) using a confocal LabRamHR spectrometer (Horiba, Villeneuve, France) equipped with a

493   liquid nitrogen–cooled CCD detector. The spectral resolution was approximately 2 cm^{-1}. Typical

494   total accumulation time and laser power at the sample were 30 min and 1 mW, respectively. Low-

495   temperature measurements at 80K were carried out with a Linkam cryostat (Linkam Scientific

496   Instruments, Surrey, UK). Samples were inserted into the cell under dimmed red light in order to

497   avoid photoactivation before freezing.

498   *MD simulations*

499   Classical MD simulations were prepared based on a SWISS homology model[71] of MerMAID1 on

500   iC++ at pH 8.5 (PDB 6CSN). The iC++ structure was chosen as template as it showed the best

501   combined quality features for structural prediction (best coverage and QMQE [0.61 together with

502   PDB 6CSM], 2nd best QSQE [0.27 vs. 0.28 with PDB 4YZI], and 3rd best identity [32.69% vs.

503   35.61% with PDB 6EID). The model was prepared using CHARMM-GUI[72] for the resting state of

504   MerMAID1 with standard protonation for all amino acids. The MerMAID1 monomer was embedded

505   inside a 60 × 60 Å, homogeneous, 1,2-dimyristoyl-sn-glycero-3-phosphocholine bilayer

506   membrane and solvated using a TIP3 water box, adding 10 Å to both the top and bottom of the

507   protein. Systems were simulated under *NPT* conditions using a 2 fs time step, a 303.15 K heat

508   bath, the particle-mesh Ewald method for long-range electrostatics, and the CHARMM36 force

509   field[73]. pK_a calculations for all titratable amino acids of MerMAID1 were performed using APBS[74]

510   in a conformational space of three pH-adapted conformations (PACs) and the Monte Carlo

511   procedure of Karlsberg2+[75,76] to sample all residues. PACs were created using Karlsberg2+ in a

512   self-consistent cycle including adjustment of protonation patterns of titratable amino acids and salt

513   bridge opening according to pH -10, 7, or 20. To calculate pK_a values for MerMAID1 MD frames,

514   only the holoprotein structure was used. Lipids and water molecules were substituted with

515   continuum solvation. Ion channels were predicted using MOLEonline[39].

516   *Neuronal recordings and two-photon microscopy*

517   Organotypic slice cultures of rat hippocampus were prepared as described[77] and transfected by

518   single-cell electroporation[78] after 14-16 days in vitro (DIV). Plasmids were each diluted to 1 ng/µl

519   in K-gluconate–based solution consisting of (in mM): 135 K-gluconate, 4 $MgCl_2$, 4 Na_2-ATP, 0.4

520   Na-GTP, 10 Na_2-phosphocreatine, 3 ascorbate, 0.02 Alexa Fluor 594, and 10 HEPES (pH 7.2).

521   An Axoporator 800A (Molecular Devices) was used to deliver 50 hyperpolarizing pulses (−12 mV,

522   0.5 ms) at 50 Hz. At DIV 19-21, targeted patch-clamp recordings of transfected neurons were

523   performed under visual guidance using a BX 51WI microscope (Olympus, Shinjuku, Japan)

524   equipped with Dodt-gradient contrast and a Double IPA integrated patch amplifier controlled with

525   SutterPatch software (Sutter Instrument, Novato, CA). Patch pipettes with a tip resistance of 3-

526   4 MΩ were filled with intracellular solution consisting of (in mM): 135 K-gluconate, 4 $MgCl_2$, 4 Na_2-

527   ATP, 0.4 Na-GTP, 10 Na_2-phosphocreatine, 3 ascorbate, 0.2 EGTA, and 10 HEPES (pH 7.2).

528   Artificial cerebrospinal fluid (ACSF) consisted of (in mM): 135 NaCl, 2.5 KCl, 2 $CaCl_2$, 1 $MgCl_2$, 10

529   Na-HEPES, 12.5 D-glucose, 1.25 NaH_2PO_4 (pH 7.4). Synaptic currents were blocked with 10 µM

530   CPPene, 10 µM NBQX, and 100 µM picrotoxin (Tocris, Bristol, UK). Measurements were

531   corrected for a liquid junction potential of -14.5 mV. A 16 channel pE-4000 LED light engine

532   (CoolLED, Andover, UK) was used for epifluorescence excitation and delivery of light pulses for

533   optogenetic stimulation (ranging from 385-635 nm). Light intensity was measured in the object

534   plane with a 1918 R power meter equipped with a calibrated 818 ST2 UV/D detector (Newport)

535   and divided by the illuminated field (0.134 mm^2) of the LUMPLFLN 60XW objective (Olympus).

536   Neurons in organotypic slice cultures were imaged with two-photon microscopy to characterize

537   their morphology and the subcellular localization of citrine-labeled MerMAID-ChRs. The custom-

538   built two-photon imaging setup was based on an Olympus BX-51WI upright microscope upgraded

539   with a multiphoton imaging package (DF-Scope, Sutter Instrument), and controlled by ScanImage

540   2017b (Vidrio Technologies, Ashburn, VA). Fluorescence was detected through the objective (NIR

541   Apo 40XW, Nikon, Minato, Japan) using GaAsP-PMTs (Hamamatsu Photonics, Hamamatsu,

542   Japan). A tunable Ti:Sapphire laser (Chameleon Vision-S, Coherent) was set to 810 nm to excite

543   mCerulean, and a high power femtosecond fiber laser (Fidelity-2, Coherent, Santa Clara, CA) was

544   used to excite citrine at 1070 nm.

545   *Data analysis and statistical methods*

546   Clampfit 10.4 (Molecular Devices) and Origin 2017 (OriginLab, Northampton, MA) were used for

547   analysis of HEK293 electrophysiological recordings. Peak currents were used for analysis of most

548   biophysical properties. The current of the last 50 ms of the illumination period was averaged to

549   determine stationary current amplitude. Reversal potentials were determined based on linear fit of

550   the two data points crossing 0 pA or linear extrapolation from 0 pA most adjacent two data points

551   of a measurement series. Action spectra were normalized to the maximum response and fitted

552   with a three-parametric Weibull function to determine the maximum response wavelength (λ_{max}).

553   Kinetic time constants were determined by mono or bi-exponential fits. For displaying reasons

554   electrophysiological recording data points were reduced.

555   Single turnover UV/vis absorption measurements were averaged over 15 cycles. Primary data

556   analysis was performed using MATLAB R2016b (The MathWorks, Natick, MA) to calculate

557   difference spectra and reconstruct three-dimensional spectra. Glotaran 1.5.1[79,80] was used for

558   global analysis of the spectral datasets. Time constant values and photointermediate spectra were

559   obtained via global analysis of the data sets. The sequential model explored spectral evolution

560   and produced the EADS, representing the species-associated difference spectra[81].

561   Stationary absorption spectra were analyzed using Origin 2017, normalized to maximum

562   absorption at 280 nm or maximum chromophore absorption, smoothed using Savitzki-Golay

563   method using a 10-point window and 5th order polynomial function. Pk_a-values were determined

564   with a Boltzmann function.

565   FTIR difference spectra were preprocessed using OPUS 7.5 software (Bruker Optics). FTIR data

566   were analyzed via single value decomposition and rotation procedure and subsequent global fit

567   algorithm implemented in Octave 4.2.[82,83]. Assuming a sequential reaction scheme, a sum of

568   exponential functions was used as the fit model.

569   RR data was background subtracted with custom written software using a polynomial function.

570   VMD[84] and PyMol 2.2.3 were used to analyze and visualize MD simulation results and computed

571   ion permeation pathways.

572   Neurophysiological data were analyzed and plotted in Igor Pro 8.0.

26

573   If not stated otherwise, data was plotted using either MATLAB, GraphPad Prism 7.0 or Origin

574   2017. Final esthetical adjustments were performed using Adobe Illustrator 2017 (Adobe Systems,

575   San José, CA) or Affinity Designer 1.6 (Serif, Nottingham, UK)

576   No statistical tests were used to predetermine sample size. Sample sizes were similar to those

577   commonly used in this research field. Repeated experiments always refer to biological replicates

578   performed using at least two batches of transfected cell cultures. Data is given as mean ± standard

579   deviation. Single measurement data and further statistical analysis[85] are provided in the

580   Supplementary Material. Blinding was not performed to ensure correct assignment of the data to

581   the measured constructs and/or experimental conditions. However, randomization was performed

582   in case of buffer exchange experiments and automated analysis was used whenever possible.

583   **Data availability**

584   HEK-293 Electrophysiological data is included in the Supplementary Material. Code and data of

585   metagenomic analysis can be obtained from https://github.com/BejaLab/MerMAIDs. Further data

586   or code is available from the corresponding authors upon request. DNA sequences will be

587   deposited on Addgene.

588   **References**

589   1.   Nagel, G. *et al.* Channelrhodopsin-1: A Light-Gated Proton Channel in Green Algae. *Science*

590   **296**, 2395–2398 (2002).

591   2.   Nagel, G. *et al.* Channelrhodopsin-2, a directly light-gated cation-selective membrane

592   channel. *Proc. Natl. Acad. Sci.* **100**, 13940–13945 (2003).

593   3.   Sineshchekov, O. A., Jung, K.-H. & Spudich, J. L. Two rhodopsins mediate phototaxis to low-

594   and high-intensity light in Chlamydomonas reinhardtii. *Proc. Natl. Acad. Sci.* **99**, 8689–8694

595   (2002).

596   4. Schneider, F., Grimm, C. & Hegemann, P. Biophysics of Channelrhodopsin. *Annu. Rev.*

597   *Biophys.* **44**, 167–186 (2015).

598   5. Lin, J. Y., Lin, M. Z., Steinbach, P. & Tsien, R. Y. Characterization of Engineered

599   Channelrhodopsin Variants with Improved Properties and Kinetics. *Biophys. J.* **96**, 1803–1814

600   (2009).

601   6. Fenno, L., Yizhar, O. & Deisseroth, K. The Development and Application of Optogenetics.

602   *Annu. Rev. Neurosci.* **34**, 389–412 (2011).

603   7. Hegemann, P., Ehlenbeck, S. & Gradmann, D. Multiple Photocycles of Channelrhodopsin.

604   *Biophys. J.* **89**, 3911–3918 (2005).

605   8. Stehfest, K. & Hegemann, P. Evolution of the Channelrhodopsin Photocycle Model.

606   *ChemPhysChem* **11**, 1120–1126 (2010).

607   9. Lórenz-Fonfría, V. A. & Heberle, J. Channelrhodopsin unchained: Structure and mechanism

608   of a light-gated cation channel. *Biochim. Biophys. Acta BBA - Bioenerg.* **1837**, 626–642

609   (2014).

610   10. Kuhne, J. *et al.* A unifying photocycle model for light adaptation and temporal evolution of

611   cation conductance in Channelrhodopsin-2. *bioRxiv* 1–29 (2018). doi:10.1101/503706

612   11. Boyden, E. S., Zhang, F., Bamberg, E., Nagel, G. & Deisseroth, K. Millisecond-timescale,

613   genetically targeted optical control of neural activity. *Nat. Neurosci.* **8**, 1263–1268 (2005).

614   12. Ishizuka, T., Kakuda, M., Araki, R. & Yawo, H. Kinetic evaluation of photosensitivity in

615   genetically engineered neurons expressing green algae light-gated channels. *Neurosci. Res.*

616   **54**, 85–94 (2006).

617   13. Li, X. *et al.* Fast noninvasive activation and inhibition of neural and network activity by

618   vertebrate rhodopsin and green algae channelrhodopsin. *Proc. Natl. Acad. Sci.* **102**, 17816–

619   17821 (2005).

620   14. Nagel, G. *et al.* Light Activation of Channelrhodopsin-2 in Excitable Cells of Caenorhabditis

621   elegans Triggers Rapid Behavioral Responses. *Curr. Biol.* **15**, 2279–2284 (2005).

15. Bi, A. *et al.* Ectopic Expression of a Microbial-Type Rhodopsin Restores Visual Responses in Mice with Photoreceptor Degeneration. *Neuron* **50**, 23–33 (2006).

16. Zhang, F. *et al.* Multimodal fast optical interrogation of neural circuitry. *Nature* **446**, 633–639 (2007).

17. Chow, B. Y. *et al.* High-performance genetically targetable optical neural silencing by light-driven proton pumps. *Nature* **463**, 98–102 (2010).

18. Wietek, J. *et al.* Conversion of Channelrhodopsin into a Light-Gated Chloride Channel. *Science* **344**, 409–412 (2014).

19. Berndt, A., Lee, S. Y., Ramakrishnan, C. & Deisseroth, K. Structure-Guided Transformation of Channelrhodopsin into a Light-Activated Chloride Channel. *Science* **344**, 420–424 (2014).

20. Wietek, J. *et al.* An improved chloride-conducting channelrhodopsin for light-induced inhibition of neuronal activity in vivo. *Sci. Rep.* **5**, (2015).

21. Berndt, A. *et al.* Structural foundations of optogenetics: Determinants of channelrhodopsin ion selectivity. *Proc. Natl. Acad. Sci.* **113**, 822–829 (2016).

22. Wietek, J. *et al.* Anion-conducting channelrhodopsins with tuned spectra and modified kinetics engineered for optogenetic manipulation of behavior. *Sci. Rep.* **7**, 14957 (2017).

23. Govorunova, E. G., Sineshchekov, O. A., Janz, R., Liu, X. & Spudich, J. L. Natural light-gated anion channels: A family of microbial rhodopsins for advanced optogenetics. *Science* **349**, 647–650 (2015).

24. Wietek, J., Broser, M., Krause, B. S. & Hegemann, P. Identification of a Natural Green Light Absorbing Chloride Conducting Channelrhodopsin from /textit{ Proteomonas sulcata}. *J. Biol. Chem.* **291**, 4121–4127 (2016).

25. Govorunova, E. G., Sineshchekov, O. A. & Spudich, J. L. Proteomonas sulcata ACR1: A Fast Anion Channelrhodopsin. *Photochem. Photobiol.* **92**, 257–263 (2016).

26. Govorunova, E. G. *et al.* The Expanding Family of Natural Anion Channelrhodopsins Reveals Large Variations in Kinetics, Conductance and Spectral Sensitivity. *Sci. Rep.* **7**, 43358 (2017).

29

648   27. Park, S. *et al.* Neuronal Allocation to a Hippocampal Engram. *Neuropsychopharmacology* **41**,

649   2987–2993 (2016).

650   28. Mahn, M., Prigge, M., Ron, S., Levy, R. & Yizhar, O. Biophysical constraints of optogenetic

651   inhibition at presynaptic terminals. *Nat. Neurosci.* **19**, 554–556 (2016).

652   29. Takahashi, N., Oertner, T. G., Hegemann, P. & Larkum, M. E. Active cortical dendrites

653   modulate perception. *Science* **354**, 1587–1590 (2016).

654   30. Mohammad, F. *et al.* Optogenetic inhibition of behavior with anion channelrhodopsins. *Nat.*

655   *Methods* **14**, 271–274 (2017).

656   31. Pushkarev, A. *et al.* A distinct abundant group of microbial rhodopsins discovered using

657   functional metagenomics. *Nature* **558**, 595–599 (2018).

658   32. Luck, M. & Hegemann, P. The two parallel Photocycles of the Chlamydomonas Sensory

659   Photoreceptor   Histidine   Kinase   Rhodopsin   1.   *J.   Plant   Physiol.*   (2017).

660   doi:10.1016/j.jplph.2017.07.008

661   33. Kouyama, T., Nishikawa, T., Tokuhisa, T. & Okumura, H. Crystal Structure of the L

662   Intermediate of Bacteriorhodopsin: Evidence for Vertical Translocation of a Water Molecule

663   during the Proton Pumping Cycle. *J. Mol. Biol.* **335**, 531–546 (2004).

664   34. Smith, S. O. *et al.* Vibrational analysis of the all-trans retinal protonated Schiff base. *Biophys.*

665   *J.* **47**, 653–664 (1985).

666   35. Bruun, S. *et al.* Light–Dark Adaptation of Channelrhodopsin Involves Photoconversion

667   between the all- trans and 13- cis Retinal Isomers. *Biochemistry* **54**, 5389–5400 (2015).

668   36. Nack, M., Radu, I., Bamann, C., Bamberg, E. & Heberle, J. The retinal structure of

669   channelrhodopsin-2 assessed by resonance Raman spectroscopy. *FEBS Lett.* **583**, 3676–

670   3680 (2009).

671   37. Smith, S. O., Pardoen, J. A., Lugtenburg, J. & Mathies, R. A. Vibrational Analysis of the 13-

672   cis-Retinal Chromophore in Dark-Adapted Bacteriorhodopsin. *J. Phys. Chem.* **91**, 804–819

673   (1987).

674   38. Kato, H. E. *et al.* Structural mechanisms of selectivity and gating in anion channelrhodopsins.

675   *Nature* **561**, 349–354 (2018).

676   39. Pravda, L. *et al.* MOLEonline: a web-based tool for analyzing channels, tunnels and pores

677   (2018 update). *Nucleic Acids Res.* **46**, W368–W373 (2018).

678   40. Joh, N. H. *et al.* Modest stabilization by most hydrogen-bonded side-chain interactions in

679   membrane proteins. *Nature* **453**, 1266–1270 (2008).

680   41. Luecke, H., Schobert, B., Richter, H.-T., Cartailler, J.-P. & Lanyi, J. K. Structure of

681   bacteriorhodopsin at 1.55 Å resolution. *J. Mol. Biol.* **291**, 899–911 (1999).

682   42. Berndt, A., Yizhar, O., Gunaydin, L. A., Hegemann, P. & Deisseroth, K. Bi-stable neural state

683   switches. *Nat. Neurosci.* **12**, 229–234 (2009).

684   43. Bamann, C., Gueta, R., Kleinlogel, S., Nagel, G. & Bamberg, E. Structural Guidance of the

685   Photocycle of Channelrhodopsin-2 by an Interhelical Hydrogen Bond. *Biochemistry* **49**, 267–

686   278 (2010).

687   44. Sineshchekov, O. A., Li, H., Govorunova, E. G. & Spudich, J. L. Photochemical reaction cycle

688   transitions during anion channelrhodopsin gating. *Proc. Natl. Acad. Sci.* **113**, E1993–E2000

689   (2016).

690   45. Bamann, C., Kirsch, T., Nagel, G. & Bamberg, E. Spectral Characteristics of the Photocycle

691   of Channelrhodopsin-2 and Its Implication for Channel Function. *J. Mol. Biol.* **375**, 686–694

692   (2008).

693   46. Lórenz-Fonfría, V. A. *et al.* Temporal evolution of helix hydration in a light-gated ion channel

694   correlates with ion conductance. *Proc. Natl. Acad. Sci.* **112**, E5796–E5804 (2015).

695   47. Li, H. *et al.* Crystal structure of a natural light-gated anion channelrhodopsin. *eLife* **8**, 1–17

696   (2019).

697   48. Schreckenbach, T., Walckhoff, B. & Oesterhelt, D. Specificity of the Retinal Binding Site of

698   Bacteriorhodopsin: Chemical and Stereochemical Requirements for the Binding of Retinol and

699   Retinal. *Biochemistry* **17**, 5353–5359 (1978).

700 49. Bruun, S. *et al.* The chromophore structure of the long-lived intermediate of the C128T

701   channelrhodopsin-2 variant. *FEBS Lett.* **585**, 3998–4001 (2011).

702 50. Oesterhelt, D. & Stoeckenius, W. Isolation of the Cell Membrane of Halobacterium halobium

703   and Its Fractionation into red and Purple Membrane. in *Methods in Enzymology* **31**, 667–678

704   (1974).

705 51. Lozier, R. H. & Niederberger, W. The photochemical cycle of bacteriorhodopsin. *Fed. Proc.*

706   **36**, 1805–9 (1977).

707 52. Govorunova, E. G., Cunha, S. R., Sineshchekov, O. A. & Spudich, J. L. Anion

708   channelrhodopsins for inhibitory cardiac optogenetics. *Sci. Rep.* **6**, 33530 (2016).

709 53. Yi, A., Mamaeva, N., Li, H., Spudich, J. L. & Rothschild, K. J. Resonance Raman Study of an

710   Anion Channelrhodopsin: Effects of Mutations near the Retinylidene Schiff Base. *Biochemistry*

711   **55**, 2371–2380 (2016).

712 54. Camacho, C. *et al.* BLAST+: architecture and applications. *BMC Bioinformatics* **10**, 421

713   (2009).

714 55. Sunagawa, S. *et al.* Structure and function of the global ocean microbiome. *Science* **348**,

715   1261359–1261359 (2015).

716 56. Brum, J. R. *et al.* Patterns and ecological drivers of ocean viral communities. *Science* **348**,

717   1261498–1261498 (2015).

718 57. Hingamp, P. *et al.* Exploring nucleo-cytoplasmic large DNA viruses in Tara Oceans microbial

719   metagenomes. *ISME J.* **7**, 1678–1695 (2013).

720 58. Philosof, A. *et al.* Novel Abundant Oceanic Viruses of Uncultured Marine Group II

721   Euryarchaeota. *Curr. Biol.* **27**, 1362–1368 (2017).

722 59. Villar, E. *et al.* The Ocean Gene Atlas: exploring the biogeography of plankton genes online.

723   *Nucleic Acids Res.* **46**, W289–W295 (2018).

724   60. Katoh, K., Rozewicki, J. & Yamada, K. D. MAFFT online service: multiple sequence alignment,

725   interactive sequence choice and visualization. *Brief. Bioinform.* 1–7 (2017).

726   doi:10.1093/bib/bbx108

727   61. Finn, R. D., Clements, J. & Eddy, S. R. HMMER web server: interactive sequence similarity

728   searching. *Nucleic Acids Res.* **39**, W29–W37 (2011).

729   62. Becker, R. A., Wilks, A. R., Brownrigg, R., Minka, T. P. & Deckmyn, A. Maps: Draw

730   Geographical Maps. (2017). Available at: https://cran.r-project.org/package=maps.

731   63. Wickham, H. *ggplot2*. (2009). doi:10.1007/978-0-387-98141-3

732   64. Rudis, B., Bolker, B., Marwick, B., Schulz, J. & Matev, R. ggalt: Extra Coordinate Systems,

733   'Geoms', Statistical Transformations, Scales and Fonts for 'ggplot2'. (2017). Available at:

734   https://cran.r-project.org/package=ggalt.

735   65. Dereeper, A. *et al.* Phylogeny.fr: robust phylogenetic analysis for the non-specialist. *Nucleic*

736   *Acids Res.* **36**, 465–9 (2008).

737   66. Larkin, M. A. *et al.* Clustal W and Clustal X version 2.0. *Bioinforma. Oxf. Engl.* **23**, 2947–2948

738   (2007).

739   67. Robert, X. & Gouet, P. Deciphering key features in protein structures with the new ENDscript

740   server. *Nucleic Acids Res.* **42**, W320–W324 (2014).

741   68. Gibson, D. G. *et al.* Enzymatic assembly of DNA molecules up to several hundred kilobases.

742   doi:10.1038/NMETH.1318

743   69. Grimm, C., Vierock, J., Hegemann, P. & Wietek, J. Whole-cell Patch-clamp Recordings for

744   Electrophysiological Determination of Ion Selectivity in Channelrhodopsins. *J. Vis. Exp.*

745   (2017). doi:10.3791/55497

746   70. Grimm, C. *et al.* Electrical properties, substrate specificity and optogenetic potential of the

747   engineered light- driven sodium pump eKR2. doi:10.1038/s41598-018-27690-w

748   71. Waterhouse, A. *et al.* SWISS-MODEL: homology modelling of protein structures and

749   complexes. *Nucleic Acids Res.* **46**, W296–W303 (2018).

72. Jo, S., Kim, T., Iyer, V. G. & Im, W. CHARMM-GUI: A web-based graphical user interface for CHARMM. *J. Comput. Chem.* **29**, 1859–1865 (2008).

73. MacKerell, A. D. *et al.* All-Atom Empirical Potential for Molecular Modeling and Dynamics Studies of Proteins. *J. Phys. Chem. B* **102**, 3586–3616 (1998).

74. Baker, N. A., Sept, D., Joseph, S., Holst, M. J. & McCammon, J. A. Electrostatics of nanosystems: Application to microtubules and the ribosome. *Proc. Natl. Acad. Sci.* **98**, 10037–10041 (2001).

75. Kieseritzky, G. & Knapp, E.-W. Optimizing pKa computation in proteins with pH adapted conformations. *Proteins Struct. Funct. Bioinforma.* **71**, 1335–1348 (2007).

76. Meyer, T. & Knapp, E.-W. pKa Values in Proteins Determined by Electrostatics Applied to Molecular Dynamics Trajectories. *J. Chem. Theory Comput.* **11**, 2827–2840 (2015).

77. Gee, C. E., Ohmert, I., Wiegert, J. S. & Oertner, T. G. Preparation of Slice Cultures from Rodent Hippocampus. 126–131 (2017). doi:10.1101/pdb.prot094888

78. Wiegert, J. S., Gee, C. E. & Oertner, T. G. Single-Cell Electroporation of Neurons. 135–139 (2017). doi:10.1101/pdb.prot094904

79. Mullen, K. M. & van Stokkum, I. H. M. TIMP : An R Package for Modeling Multi-way Spectroscopic Measurements. *J. Stat. Softw.* **18**, (2007).

80. Snellenburg, J. J., Laptenok, S. P., Seger, R., Mullen, K. M. & van Stokkum, I. H. M. Glotaran: A Java-Based Graphical User Interface for the R Package TIMP. *J. Stat. Softw.* **49**, 1–22 (2012).

81. Toh, K. C., Stojkovic, E. A., van Stokkum, I. H. M., Moffat, K. & Kennis, J. T. M. Proton-transfer and hydrogen-bond interactions determine fluorescence quantum yield and photochemical efficiency of bacteriophytochrome. *Proc. Natl. Acad. Sci.* **107**, 9170–9175 (2010).

82. Elgeti, M., Ritter, E. & Bartl, F. J. New Insights into Light-Induced Deactivation of Active Rhodopsin by SVD and Global Analysis of Time-Resolved UV/Vis- and FTIR-Data. *Z. Für Phys. Chem.* **222**, 1117–1129 (2008).

776   83. Henry, E. R. & Hofrichter, J. Singular value decomposition: Application to analysis of
777   experimental data. in *Methods in Enzymology* **210**, 129–192 (1992).

778   84. Humphrey, W., Dalke, A. & Schulten, K. VMD: Visual Molecular Dynamics. *J. Mol. Graph.* **14**,
779   33–38 (1996).

780   85. Ho, J., Tumkaya, T., Aryal, S., Choi, H. & Claridge-Chang, A. Moving beyond P values:
781   Everyday data analysis with estimation plots. *bioRxiv* **6**, 377978 (2018).

782   86. Pinhassi, J., DeLong, E. F., Béjà, O., González, J. M. & Pedrós-Alió, C. Marine Bacterial and
783   Archaeal Ion-Pumping Rhodopsins: Genetic Diversity, Physiology, and Ecology. *Microbiol.*
784   *Mol. Biol. Rev.* **80**, 929–954 (2016).

785

Acknowledgments

Author Contributions

798   J.W., J.O., and P.He. designed the project, with contributions from all authors. J.F.-U., E.P., I.S.,
799   O.B., J.W., and J.O. performed computational work. J.O., B.L., S.R-R., P.F., A.S., A.K., and J.V.

800   conducted the experiments, with assistance from M.B. and M.L. Experimental data were analyzed

801   by J.O., J.W., B.L., S.R-R., P.F., A.S., and A.K. and interpreted by all authors. J.W., J.O., and

802   P.He. wrote the manuscript, with contributions from all authors.

803   **Competing Interests**

804   The authors declare no competing interests.